Accelerating Dynamic Spiral MRI by Algebraic Reconstruction From Undersampled k–t Space

Taehoon Shin*, *Student Member, IEEE*, Jon-Fredrik Nielsen, *Member, IEEE*, and Krishna S. Nayak, *Member, IEEE*

Abstract—The temporal resolution of dynamic magnetic resonance imaging (MRI) can be increased by sampling a fraction of k-space in an interleaved fashion, which introduces spatial and temporal aliasing. We describe algebraically and graphically the aliasing process caused by dynamic undersampled spiral imaging within 3-D xyf space (the Fourier transform of $k_x k_y t$ space) and formulate the unaliasing problem as a set of independent linear inversions. Since each linear system is numerically underdetermined, the use of prior knowledge in the form of bounded support regions is proposed. To overcome the excessive memory requirements for handling large matrices, a fast implementation of the conjugate gradient (CG) method is used. Numerical simulation and *in vivo* experiments using spiral twofold undersampling demonstrate reduced motion artifacts and the improved depiction of fine cardiac structures. The achieved reduction of motion artifacts and motion blur is comparable to simple filtering, which is computationally more efficient, while the proposed algebraic framework offers greater flexibility to incorporate additional algebraic acceleration techniques and to handle arbitrary sampling schemes.

Index Terms—Algebraic reconstruction, dynamic imaging, fast imaging, spiral cardiac magnetic resonance imaging (MRI), temporal acceleration.

I. INTRODUCTION

DYNAMIC magnetic resonance imaging (MRI), which captures temporal variations of objects of interest, is receiving increasing interest as an effective diagnostic tool. It has been proven to be particularly useful for cardiac imaging since the human heart involves a high degree of dynamic motion [1], [2]. Cardiac gated scanning during a breathhold can achieve high spatial and temporal resolutions but is affected by arrhythmias and the breathhold requirements. In some cases, the aperiodic pattern itself may represent actual diagnostic information. Recent advances in MR hardware and pulse sequences have made it possible to perform dynamic cardiac imaging without gating or breathhold [3]. However, many applications still demand higher temporal resolution, which has remained an important research topic.

One way to increase the temporal resolution of dynamic MRI is by sampling only a fraction of k-space. The fundamental principle of these methods is to exploit information redundancy, and they can be divided into two groups based on the source of the redundancy. The first group includes partial k-space reconstruction [4] and parallel imaging [5]–[7], where the redundancy source is inherent properties of the image or external hardware. Dynamic properties of moving objects are irrelevant to these methods, and they can be applied to both static and dynamic imaging. The second group utilizes information redundancy from temporal correlations of dynamic images. Keyhole methods and reduced-encoding MR imaging by generalized-series reconstruction (RIGR) assume that temporal variation is primarily from the central portion of k-space [8]–[10]. Similarly, reduced field-of-view (FOV) reconstruction utilizes the fact that only a limited region of an image undergoes substantial variation over time [11]–[13]. That is, the information from relatively stationary regions in object space is considered to be redundant.

The second group, introduced above, was advanced by a novel reconstruction based on temporal filtering called UNaliasing by Fourier-encoding the Overlaps using the temporaL Dimension (UNFOLD) [14], [15]. By undersampling k-space in an interleaved fashion over time, UNFOLD displaces aliased signals along the frequency axis and recovers the original signal using a temporal low-pass filter. Further acceleration is achievable with the k–t broad-use linear acquisition speed-up technique (k–t BLAST), which uses training data as prior information along with the interleaved sampling function [16]. Conceptually, UNFOLD and k–t BLAST reduce the information redundancy by economically using k–t space (the combination of k-space with a time axis [17]). Until now, these two methods have been used mainly with Cartesian k-space trajectories, due to the simplicity of describing and correcting for the aliasing produced by rectilinear sampling patterns (refer to [18] as a non-Cartesian example). However, spiral readouts are appropriate for certain applications because they have good flow properties [19] and are time efficient, which enables further increases in spatial and/or temporal resolution when used in conjunction with undersampling techniques.

In this paper, we describe the aliasing process for spiral sampling trajectories and formulate unaliasing as an inverse problem in 3-D xyf space, the transform of $k_x k_y t$ space. In general, any aliasing caused by the violation of the Nyquist condition cannot be resolved under arbitrary condition, which manifests, in our case, as numerically underdetermined system matrices. We show that the aliasing is formed such that only a few temporal frequency components are coupled, and the rank deficiency problem is isolated in each set of temporal frequencies. From the fact that the support region is bounded in xyf space, a zero assumption in the solutions is used to condition each linear system. We inspect how the size and the location of assumed zeros affect the degree of rank deficiency by borrowing ideas from the Cartesian undersampling case.

*T. Shin is with the University of Southern California, Los Angeles, CA 90089 USA (e-mail: taehoons@usc.edu).

J.-F. Nielsen and K. S. Nayak are with the University of Southern California, Los Angeles, CA 90089 USA.
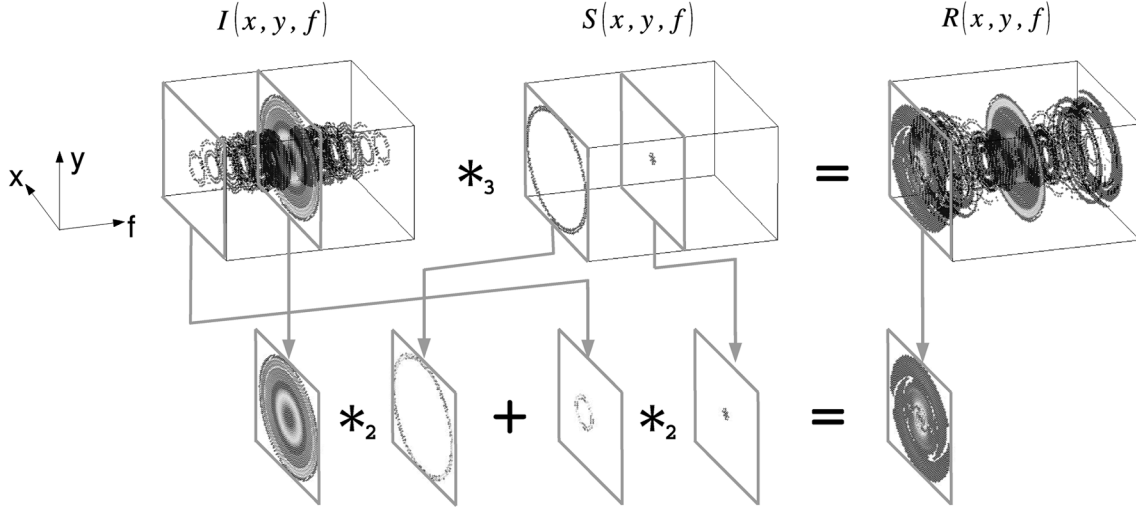
Fig. 1. Illustration of dynamic undersampled spiral imaging in xyf space. From twofold undersampling, ring-shaped sidelobes are shifted to the Nyquist frequency. Since mainlobe and sidelobes are confined to dc and the Nyquist frequency respectively, the solutions of only two temporal frequencies are coupled to generate aliasing at one temporal frequency.

Finally, the proposed method is validated through numerical simulations and *in vivo* spiral cardiac MRI experiments.

II. THEORY

During dynamic MRI, k-space data of moving objects are acquired according to a specific sampling function at different time points. The $k_x k_y t$ space should be considered as the working space of data acquisition in which a sampled object $R_{k_x k_y t}$ is expressed as an original object $I_{k_x k_y t}$ multiplied by a sampling function $S_{k_x k_y t}$

$$I_{k_x k_y t}(k_x, k_y, t) \cdot S_{k_x k_y t}(k_x, k_y, t) = R_{k_x k_y t}(k_x, k_y, t). \quad (1)$$

In the reciprocal domain called xyf space, the above relation becomes

$$I_{xyf}(x, y, f) *_3 S_{xyf}(x, y, f) = R_{xyf}(x, y, f) \quad (2)$$

where $S_{xyf}(x, y, f) = \mathcal{F}_3^{-1}(S_{k_x k_y t})$, the 3-D inverse Fourier transform of the sampling function, is a point spread function (PSF), and $*_3$ denotes the 3-D convolution operator. In the rest of this paper, all operations are in xyf space and the subscript xyf will be omitted.

When a fraction of k-space is scanned in a time-interleaved fashion, the PSF sidelobe has different phase at successive time points, with the pattern depending on the acquisition order. Aliased signals are shifted along the temporal frequency axis, which makes it easier to separate the original signal from the aliased ones. The modulation phenomenon of the PSF can be proved in a straightforward way in Cartesian undersampling [14]. Particularly in twofold undersampling, segmenting an arbitrary k-space trajectory which satisfies the Nyquist condition into two subsets and sampling them alternately will lead to modulation of the PSF. Since the summation of the two subsets induces only mainlobe within FOV, the two PSF sidelobes should amount to zero, which means that the two sidelobes have opposite phases.

The top of Fig. 1 shows an example object, the PSF associated with spiral twofold undersampling, and the corresponding aliasing pattern in 3-D xyf space. It is assumed that only the central part of the object is moving. Once the PSF is described in this 3-D space, the resulting aliasing can be understood as a 3-D convolution of the original object with its mainlobe and sidelobes.

A. Algebraic Formulation of Aliasing

The 3-D convolution (2) can be formulated as a linear matrix system. However, solving the inversion problem as a whole is impractical on a conventional workstation due to memory requirements. Also, the sparseness of the PSF remains unexplored in the 3-D convolution formulation. Because of the temporal modulation of the PSF in twofold undersampling, the mainlobe and sidelobe are strictly confined to dc and the Nyquist frequency, respectively, as shown in Fig. 1. Then, we can express the 3-D convolution as

$$\begin{aligned} R(x, y, f) &= \sum_{l=0}^{L-1} \sum_{p=0}^{N-1} \sum_{q=0}^{N-1} [I(p, q, l)S(x - p, y - q, f - l)] \\ &= \sum_{l=0}^{L-1} \left[\sum_{p=0}^{N-1} \sum_{q=0}^{N-1} I^{(l)}(p, q)S^{(f-l)}(x - p, y - q) \right] \\ &= \sum_{l=0}^{L-1} \left[I^{(l)} *_2 S^{(f-l)} \right] \\ &= I^{(f)} *_2 S^{(0)} + I^{(f-\frac{L}{2})} *_2 S^{(\frac{L}{2})} \quad (3) \end{aligned}$$

where $I^{(l)}$ and $S^{(l)}$ denote the original signal and the PSF at temporal frequency $f = l$, and $*_2$ denotes 2-D linear convolution. In the third line of (3), the initial 3-D convolution is expressed as the summation of 2-D convolutions. Furthermore, only two temporal frequency terms ($S^{(0)}$ and $S^{(L/2)}$) are nonzero, and the equation therefore reduces to the last expression in (3).

If the 2-D convolution matrices associated with $S^{(0)}$ and $S^{(L/2)}$ are $\mathbf{A}_1$ and $\mathbf{A}_2$, the aliasing from twofold undersampling can be written as

$$\begin{bmatrix} \mathbf{A}_1 & \mathbf{A}_2 \\ \mathbf{A}_2 & \mathbf{A}_1 \end{bmatrix} \begin{bmatrix} \mathbf{x}_l \\ \mathbf{x}_{l+\frac{L}{2}} \end{bmatrix} = \begin{bmatrix} \mathbf{b}_l \\ \mathbf{b}_{l+\frac{L}{2}} \end{bmatrix} \quad l = 0, 1, \ldots, L/2 - 1 \tag{4}$$

where $\mathbf{x}_l = (I^{(l)})_{N \times N \to N^2 \times 1}$ and $\mathbf{b}_l = (R^{(l)})_{N \times N \to N^2 \times 1}$, i.e., $N^2 \times 1$ column vectors in which the elements of $I^{(l)}$ and $R^{(l)}$ are stacked in a raster-like fashion. Note that only two temporal frequencies $I^{(l)}$ and $I^{(l+(L/2))}$ are coupled into the same linear system. For example, the aliasing at the Nyquist frequency is generated from the dc and the Nyquist frequency components which are convolved with the mainlobe and the sidelobe, respectively (see bottom of Fig. 1).

The generalization of this algebraic formulation into higher order undersampling is straightforward. The PSF from m-fold undersampling contains nonzero signals at only m temporal frequencies $f = 0, (L/m), \cdots, (m - 1/m)L$. If we represent the corresponding 2-D convolution matrices as $\mathbf{A}_1, \mathbf{A}_2, \cdots, \mathbf{A}_m$, then the generalized version of (4) is written as

$$\begin{bmatrix} \mathbf{A}_1 & \mathbf{A}_m & \ldots & \mathbf{A}_2 \\ \mathbf{A}_2 & \mathbf{A}_1 & \ldots & \mathbf{A}_3 \\ \vdots & \vdots & \ddots & \vdots \\ \mathbf{A}_m & \mathbf{A}_{m-1} & \ldots & \mathbf{A}_1 \end{bmatrix} \begin{bmatrix} \mathbf{x}_l \\ \mathbf{x}_{l+\frac{L}{m}} \\ \vdots \\ \mathbf{x}_{l+\frac{m-1}{m}L} \end{bmatrix} = \begin{bmatrix} \mathbf{b}_l \\ \mathbf{b}_{l+\frac{L}{m}} \\ \vdots \\ \mathbf{b}_{l+\frac{m-1}{m}L} \end{bmatrix} \tag{5a}$$

or

$$\mathbf{x}^{(l)} = \mathbf{b}^{(l)} \quad l = 0, 1, \cdots, \frac{L}{m} - 1. \tag{5b}$$

The solution of every (L/m)th frequency is coupled into the same linear system, and a total of (L/m) such systems can be solved independently.

In general, the aliasing described by (2) cannot be easily resolved since the corresponding linear equations are ill posed. The separability of the solutions in (4) and (5) indicates the insufficient rank problem is isolated in each set of aliased temporal frequencies. The next section discusses a method to condition each set of equations.

B. Rank Analysis and Zero Assumption

The existence of a unique solution to (5) is directly related to the rank of the system matrix $\mathbf{A}$. The solution can be uniquely determined only if the rank of the system matrix is equal to the number of unknowns. The direct rank analysis of the system matrix associated with spiral undersampling is quite complicated due to the complexity of its PSF. To obtain intuition about rank deficiency, we will borrow ideas from Cartesian twofold undersampling and show that the degree of rank deficiency depends on the overlapped area between the nonzero signals at two aliased temporal frequencies.

Fig. 2 shows the image view of the system matrix defined in (4) associated with the Cartesian twofold undersampling and the corresponding solutions $I^{(l)}$ and $I^{(l+(L/2))}$. $\mathbf{A}_1$ is diagonal and $\mathbf{A}_2$ has two off-diagonal lines since $S^{(0)}$ has one impulse
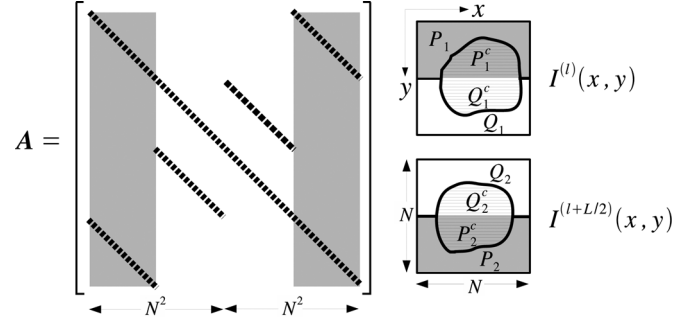

Fig. 2. Illustration of the system matrix in Cartesian twofold undersampling with the solution for two coupled temporal frequencies. Rank is half the matrix dimension since the first and fourth quarter-columns (gray) are identical, and the second and third quarter-columns (white) are identical. To condition rank deficiency, zeros can be assumed in certain regions of solution. P_k and $Q_k(k = 1, 2)$ represent region of zero assumption. Accordingly, $P_k{}^c$ and $Q_k{}^c(k = 1, 2)$ represent support regions of solution.

at the object domain origin and $S^{(L/2)}$ has two impulses at the edge in the phase encoding direction. The rank of $\mathbf{A}$ is exactly half the matrix dimension. Assuming $I^{(l)}$ has the size of $N \times N$ and thus the dimension of $\mathbf{A}$ is $2N^2 \times 2N^2$, the first-quarter columns of dimension $2N^2 \times (N^2/2)$ are the same as the last quarter columns, and the second quarter columns are the same as the third quarter. These repeated columns indicate that the overlap between the upper (or lower) half of $I^{(l)}$ and the lower (or upper) half of $I^{(l+(L/2))}$ occurs in both $R^{(l)}$ and $R^{(l+(L/2))}$. Consequently, any aliased position forms a pair with another location to produce a single effective rank.

A good candidate for mitigating this rank deficiency is assuming zeros in a certain region of the solution since the solution's support region is bounded in xyf space. Then, the columns of the system matrix corresponding to the position of zero assumption will be discarded. A key question about this assumption is the effect of the size and the location of assumed zeros on the rank deficiency. For notational convenience, we define four sets of zero locations P_k and $Q_k(k = 1, 2)$ and four sets of the corresponding support regions $P_k{}^c$ and $Q_k{}^c(k = 1, 2)$ (Fig. 2)

$$P_1 \equiv \left\{ (x, y) \mid I^{(l)}(x, y) = 0, 0 \le y \le \frac{N}{2} - 1 \right\}$$

$$P_2 \equiv \left\{ (x, y) \mid I^{(l+\frac{L}{2})}(x, y) = 0, \frac{N}{2} \le y \le N - 1 \right\}$$

$$Q_1 \equiv \left\{ (x, y) \mid I^{(l)}(x, y) = 0, \frac{N}{2} \le y \le N - 1 \right\}$$

$$Q_2 \equiv \left\{ (x, y) \mid I^{(l+\frac{L}{2})}(x, y) = 0, 0 \le y \le \frac{N}{2} - 1 \right\} \tag{6}$$

$$P_1{}^c \equiv \left\{ (x, y) \mid I^{(l)}(x, y) \ne 0, 0 \le y \le \frac{N}{2} - 1 \right\}$$

$$P_2{}^c \equiv \left\{ (x, y) \mid I^{(l+\frac{L}{2})}(x, y) \ne 0, \frac{N}{2} \le y \le N - 1 \right\}$$

$$Q_1{}^c \equiv \left\{ (x, y) \mid I^{(l)}(x, y) \ne 0, \frac{N}{2} \le y \le N - 1 \right\}$$

$$Q_2{}^c \equiv \left\{ (x, y) \mid I^{(l+\frac{L}{2})}(x, y) \ne 0, 0 \le y \le \frac{N}{2} - 1 \right\}. \tag{7}$$

Then, the matrix rank r and the number of unknowns y are expressed as

$$r = N^2 - (|P_1 \cap P_2| + |Q_1 \cap Q_2|)$$
$$y = 2N^2 - (|P_1| + |P_2| + |Q_1| + |Q_2|). \qquad (8)$$

The degree of rank deficiency can be written as

$$r - y = |P_1 \cup P_2| + |Q_1 \cup Q_2| - N^2$$
$$= |(P_1{}^c \cap P_2{}^c)^c| + |(Q_1{}^c \cap Q_2{}^c)^c| - N^2$$
$$= -|P_1{}^c \cap P_2{}^c| - |Q_1{}^c \cap Q_2{}^c|. \qquad (9)$$

In Cartesian twofold undersampling, the upper half and the lower half of $I^{(l)}$ are superimposed with the lower half and the upper half of $I^{(l+(L/2))}$, respectively. Since $|P_1{}^c \cap P_2{}^c|$ and $|Q_1{}^c \cap Q_2{}^c|$ represent the area of the overlap between nonzero signals of $I^{(l)}$ and $I^{(l+(L/2))}$, (9) tells us that the degree of rank deficiency depends on the size of this overlapped region.

In this paper, these properties are assumed to carry over into the spiral undersampling without a rigorous proof. Since the sidelobe of the spiral undersampling is ring shaped, the radial extents of the support regions in $I^{(l)}$ and $I^{(l+(L/2))}$ are critical to the overlapping area. Hence, a support region of circular shape will be used for specifying the zero assumption in each $I^{(l)}$.

The zero assumption, in its function, is similar to the temporal filtering used in UNFOLD. It should be noticed that the solutions are obtained from the algebraic processes, which enables incorporation of additional algebraic operation into the proposed framework. The regularization mentioned in the next section can be considered as a simple form of such incorporation.

C. Pseudoinverse and Regularization

With the zero assumption, the linear system becomes overdetermined and the conventional inverse does not exist. The optimal solution in the minimum norm least square sense can be obtained by solving the normal equation $\mathbf{A}^H \mathbf{A} \mathbf{x} = \mathbf{A}^H \mathbf{b}$. $(\mathbf{A}^H \mathbf{A})^{-1}$ can be computed only if all columns of $\mathbf{A}$ are independent. However, $\mathbf{A}^H \mathbf{A}$ will still be ill posed when the size of the zero assumption is insufficient.

We need regularization which changes the original problem such that the modified system becomes stable while still being reasonably close to the original one. We use a popular type of regularization called Tikhonov filtering which produces a regularized linear system written as

$$(\mathbf{A}^H \mathbf{A} + \rho \mathbf{I}) \mathbf{x} = \mathbf{A}^H \mathbf{b} \qquad (10)$$

where the regularization coefficient ρ balances the tradeoff between solution stability and accuracy. The addition of $\rho \mathbf{I}$ is equivalent to replacing the original cost function with $\|\mathbf{A}\mathbf{x} - \mathbf{b}\|^2 + \rho \|\mathbf{x}\|^2$, which adds weighting on the norm of the solution vector.

D. Iterative Solution

With a reconstructed image of $N \times N$ pixels, the dimension of the system matrix with twofold undersampling will be $(2N^2) \times (2N^2)$ as seen from (4). Moreover, the number of operations required for direct computation of its inverse is of order $O(N^6)$.

One common way to overcome this obstacle is using an iterative method to solve the inverse problem. In this paper, the conjugate gradient (CG) method, a classical iterative algorithm, is used. It is well known that CG guarantees an exact solution only if the system matrix is symmetric and positive definite, which can be easily proved for the regularized system matrix $\mathbf{A}^H \mathbf{A} + \rho \mathbf{I}$.

The most computationally demanding part in each kth iteration of CG is the matrix-vector multiplication $(\mathbf{A}^H \mathbf{A} + \rho \mathbf{I})\mathbf{x}^{(k)}$ which requires the storage of $(2N^2 \times 2N^2)$ complex matrices and $O(N^4)$ operations. Since the product $\mathbf{A}\mathbf{x}$ originates from the combination of several 2-D convolutions as described in (3) and (4), it can be rewritten as

$$\mathbf{A}\mathbf{x} = \begin{bmatrix} \mathbf{A}_1 \mathbf{x}_l + \mathbf{A}_2 \mathbf{x}_{l+\frac{L}{2}} \\ \mathbf{A}_2 \mathbf{x}_l + \mathbf{A}_1 \mathbf{x}_{l+\frac{L}{2}} \end{bmatrix}$$
$$= \begin{bmatrix} \left(S^{(0)} *_2 I^{(l)} + S^{(\frac{L}{2})} *_2 I^{(l+\frac{L}{2})} \right)_{N \times N \to N^2 \times 1} \\ \left(S^{(\frac{L}{2})} *_2 I^{(l)} + S^{(0)} *_2 I^{(l+\frac{L}{2})} \right)_{N \times N \to N^2 \times 1} \end{bmatrix}. \qquad (11)$$

Each of the four 2-D convolutions involved in (11) can be computed by

$$S *_2 I = \mathcal{F}_2^{-1}[\mathcal{F}_2(S)\mathcal{F}_2(I)] \qquad (12)$$

where $\mathcal{F}_2$ and $\mathcal{F}_2^{-1}$ denote the forward and the backward 2-D Fourier transforms and all superscripts are discarded for brevity.

The additional multiplication with $\mathbf{A}^H$ can be computed in a similar way. Since 2-D FFT has the complexity of $O(N^2 \log N)$, the computational load at each iteration can be reduced by a factor of $O(N^2/\log N)$.

One should pay attention to the boundary effects of linear convolutions denoted by $*_2$ above. The PSF $S^{(0)}$ and $S^{(L/2)}$ have infinitely many sidelobes along the radial direction. If only the nominal FOV (of size $N \times N$) is taken and convolved with the solutions $I^{(l)}$ and $I^{(l+(L/2))}$, the signal produced by the sidelobe outside the FOV will be ignored. Assuming that all nonzero signals exist within the FOV, including the sidelobes within $2 \times$ FOV will be enough for handling all aliased signals introduced in the FOV. For the implementation of the 2-D convolutions, the PSF of $2 \times$ FOV ($2N \times 2N$) is prepared and the solution $I^{(l)}$ is zero-padded to generate a $2 \times$ FOV image. After computing the extended $2 \times$ FOV convolutions using (12), desired convolutions free of boundary effects can be obtained by cropping the $2 \times$ FOV convolution results.

III. METHODS

A. Numerical Phantom Simulation

A dynamic numerical phantom was used for the validation of the proposed method applied to spiral twofold undersampling. The phantom, which resembles a short axis cardiac image, includes a chest wall, right and left ventricles, a myocardium, and papillary muscles represented by two dots (Fig. 3). The ventricles and the myocardium keep contracting and expanding periodically based on the cosine function with period 1 s. The outer and inner diameters of the myocardium change such that the area of the myocardium should be conserved. A total of six spiral interleaves are used with a matrix size of 128×128. Each
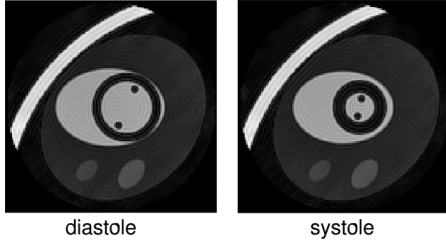
Fig. 3.   Diastolic and systolic phases of the dynamic numerical phantom. The phantom was designed to resemble the heart in a short axis view, with the size of the left ventricle changing sinusoidally.
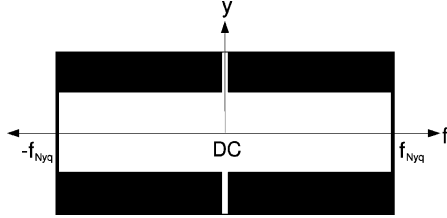

Fig. 4.   Cross-sectional view of zero assumption in numerical phantom study. The support region is cylindrical in xyf space.

Fig. 5.   Cross-sectional view of the zero assumption in *in vivo* experiments. The support region resembles a truncated cone in xyf space.

set of odd and even order interleaves is assumed to be sampled simultaneously so that motion artifacts within each set are being neglected. The time interval between each set of interleaves is set to 48 ms which produces, for a heart rate of 60 beats per minute, roughly 21 frames per cardiac cycle from twofold acceleration. For error quantification, we use the maximum error and the normalized root-mean-square (rms) error expressed as

$$E_{\mathrm{RMS}}^{(t)} = \sqrt{\frac{\sum_{i=0}^{N-1}\sum_{j=0}^{N-1}\left|r_{i,j}^{(t)} - o_{i,j}^{(t)}\right|^2}{\sum_{i=0}^{N-1}\sum_{j=0}^{N-1}\left|o_{i,j}^{(t)}\right|^2}} \qquad (13)$$

where $E_{\mathrm{RMS}}^{(t)}$ denotes rms error at time t. $r_{i,j}^{(t)}$ and $o_{i,j}^{(t)}$ represent the (i,j)th pixel intensity of the reconstructed image and the true image at time t, respectively.

The cross-sectional view of the zero assumption is shown in Fig. 4. Since we know that the most dynamic part of the phantom lies inside half the FOV, the remaining outer region is assumed to be zero, which can be applied to all pairs of $I^{(l)}$ and $I^{(l+(L/2))}$, except dc and the Nyquist frequency ($l = 0$). The whole region of $I^{(0)}$ must be nonzero and $I^{(L/2)}$ is likely to have small nonzero values in its support region. In this case, the area of assumed zeros is insufficient and the corresponding system matrix will be ill posed. In this paper, we simply assume that $I^{(L/2)}$ is zero and take the dc of the aliased signal $R^{(0)}$ as the solution of $I^{(0)}$.

For comparison purposes, reference images were generated using sliding window reconstruction [20] and UNFOLD-like filtering which does not involve algebraic inversion. To make the reconstruction time points of the sliding window reconstruction coincide with those of UNFOLD-like filtering and the proposed method, the image at each time point is generated from the raw data at the current time point and the average of the raw data from th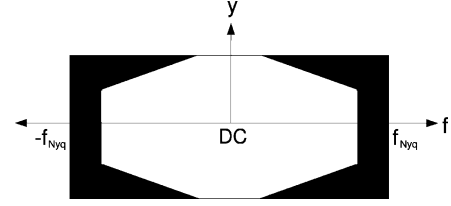e previous and next time points. UNFOLD-like filtering is implemented using the same support region in xyf space shown in Fig. 4.

B. In Vivo Experiments

Experiments were performed on a 1.5-T GE Signa EXCITE system, with 22-mT/m maximum gradient amplitude and 77-T/m/s maximum slew rate. A phased array coil with four channels was used for signal reception, and the raw data from two channels were used for reconstruction. Real-time (free breathing and ungated) spiral balanced SSFP cardiac imaging was conducted [21]. The imaging protocol used 36 spiral interleaves, an in-plane resolution of 2.4×2.4 mm, a slice thickness of 10 mm, a $60°$ flip angle, and a repetition time (TR) of 6.4 ms. The gradient waveforms were designed such that both the zeroth and first moments are zero between RF pulses to ensure steady-state signal coherence and to avoid in-plane flow effects. A total of 100 image frames were reconstructed from the proposed method, which used a set of odd or even order interleaves alternately to form one image frame.

Since the numerical rank of the system matrix depends on the radial extents of the support region in $I^{(l)}$, as mentioned in Section II, it is reasonable to use a stack of circles for the zero assumption in xyf space. Then, the design parameter to be determined is the profile of the diameters along the frequency axis. In this paper, a ramp-shaped profile was used, assuming the temporal variation of images to be dominant in the central region (Fig. 5). Note that the high frequency region, which amounts to 16% of the whole bandwidth, is filtered out since in this band there will be strong aliased signals arising from the sidelobe. The linear systems associated with the zero assumption displayed in Fig. 5 will be slightly ill posed. We observe that this loose zero assumption produces more robust results than a tight support region which enables better conditioning but fails to truly contain all nonzero signals. Reference images were generated using the sliding window reconstruction and UNFOLD-like filtering which used the same support region shown in Fig. 5.

IV. RESULTS

A. Numerical Phantom Simulation

Normalized rms errors, maximum errors, reconstructed images, and residue images from the sliding window reconstruction, UNFOLD-like filtering, and the proposed method are shown in Fig. 6. The proposed method produces smaller errors than the sliding window reconstruction in terms of both rms and maximum values. The proposed method produces comparable but smaller errors compared to UNFOLD-like filtering. The largest improvement is in maximum errors because of
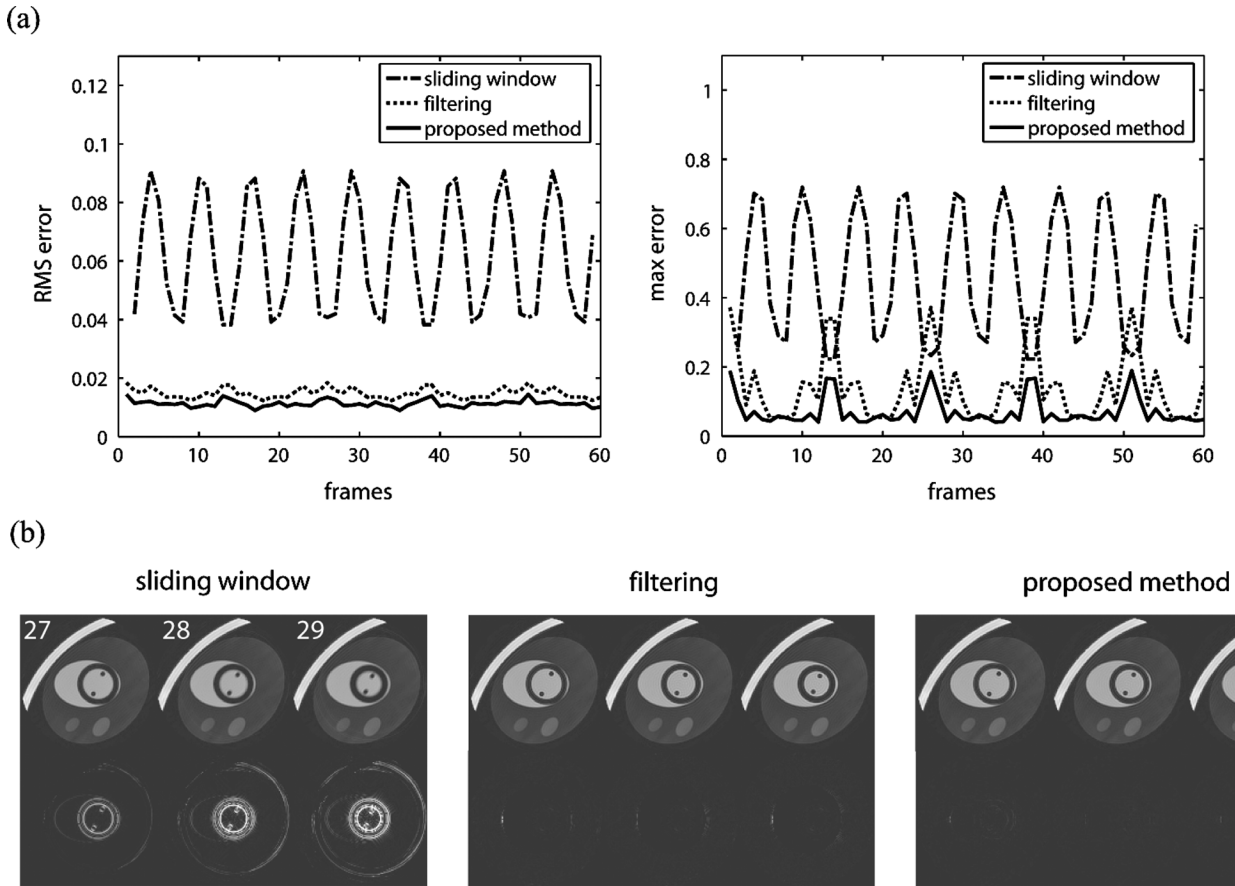
(a)

(b)

Fig. 6. Simulated phantom results using sliding window reconstruction, UNFOLD-like filtering, and the proposed method. (a) Normalized rms error and maximum pixel-by-pixel error illustrate that the proposed method has smaller error than sliding window reconstruction. Compared to filtering, slight improvements are observed because of regularization effects. There is a large periodic increase in error in sliding window reconstruction when motion is the fastest (twice per cycle). Periodic increase in errors for filtering and the proposed method is related to the size of the dynamic region approaching the edge of the support region at diastolic phases (once per cycle). (b) Representative reconstructed images and residue images from the three consecutive frames are shown for three reconstructions. Residue images are defined as the difference between the reconstructed images and the known true images and are displayed using harsh windowing.

regularization effects. The large error fluctuation of the sliding window reconstruction arises from the fact that the ventricle and myocardium signals change sinusoidally. The motion artifacts are small around the time points of the maximum and the minimum of the cosine and large at phases between them. The image of frame number 29 that corresponds to the highest slope of the cosine function shows the largest motion blurring, which is verified by the corresponding residue image. Using filtering and the proposed method, the temporal blurring of moving structures is reduced due to increased temporal resolution.

Filtering and the proposed reconstruction produce small periodic error fluctuations which have local maxima at each diastole. In diastole, when the simulated heart is at its widest, the extent of the dynamic region exceeds the specified support region. In this simulation, the periodic error increase is the result of an incorrect zero assumption which designates some nonzero pixels outside the support region.

B. In Vivo Experiments

Fig. 7(a) shows systolic short axis images (20th frame) reconstructed from sliding window reconstruction, UNFOLD-like filtering, and the proposed method. The image difference is subtle, but a slight improvement can be found from the examination of fine cardiac structures. Fig. 7(b) shows the signal intensity pro-

files through the moderator band in the right ventricle. The paths of the signal profiles are the missing parts of the horizontal and vertical lines shown in Fig. 7(a). The band is most sharply captured using the proposed method, followed by filtering, and finally sliding window, which matches the expected order of least motion blur to most motion blur.

Another set of systolic short axis images (59th frame) is shown in Fig. 7(c) using harsh windowing to visualize motion artifacts which appear as background whirling. The average signal intensity in the region of interest (ROI), specified by the dotted box, is plotted as a function of time in Fig. 7(d). The mean values fluctuate at the heart rate, which implies that the artifacts in the ROI relate to cardiac motion. The proposed method reduces motion artifacts as well as UNFOLD-like filtering compared to sliding window reconstruction.

Reconstruction was performed in MATLAB on a Dell 8400 desktop computer (3.6 GHz Intel processor, 1 GB RAM). Proposed reconstruction of 100 temporal frames, using two coils, required approximately 5 min of CPU time.

V. DISCUSSION

The most critical component in the implementation of the proposed method is determining the shape of the zero assumption in xyf space. If the zero assumption is insufficient (i.e., the
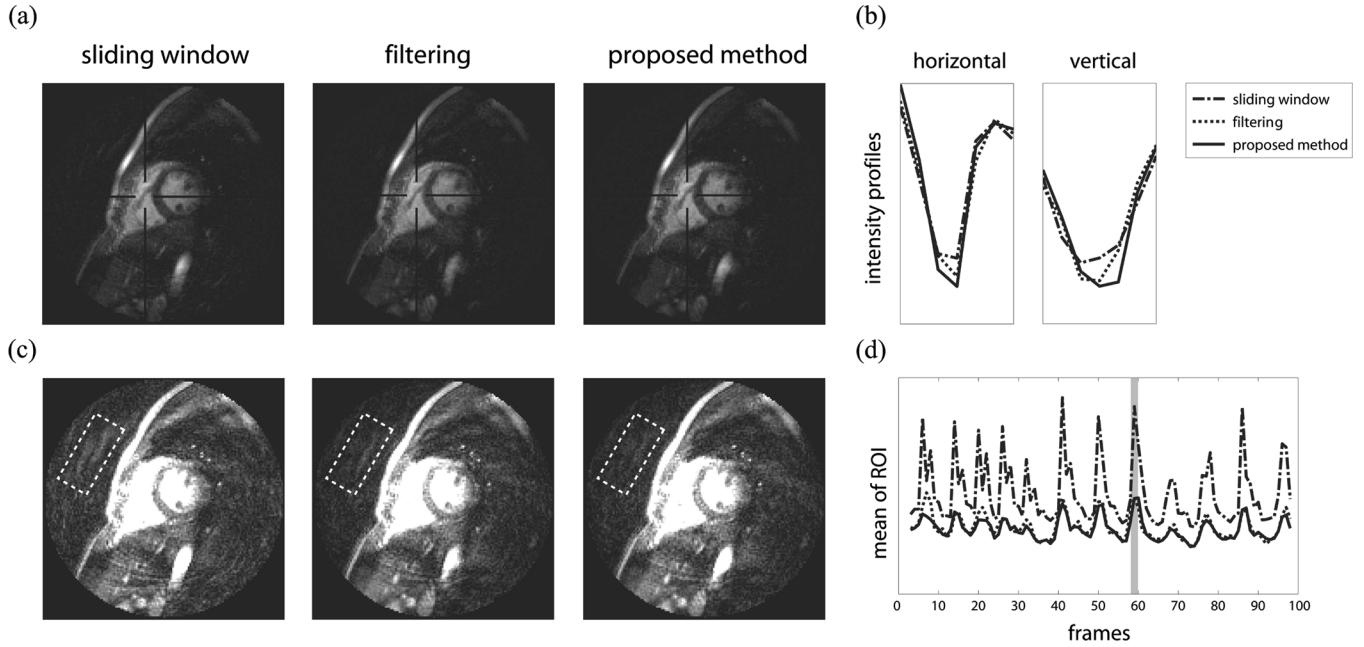
(a)

(b)

Fig. 7. *In vivo* experiment results using sliding window reconstruction, UNFOLD-like filtering, and the proposed method. (a) To evaluate improvement in the depiction of fine cardiac structures, signal profiles across the moderator band of the right ventricle (black cross-hairs) were measured (20th time frame). (b) Intensity profiles indicate sharp depiction of the moderator band in the order of the proposed method, filtering, and the sliding window. (c) To visualize motion artifact reduction, short axis images from the three methods were windowed harshly (59th time frame) and signal in a region outside of the body (white box) was measured. (d) Mean signal within the box is plotted as a function of time illustrating that the proposed method reduces motion artifacts as well as filtering.

diameters of the circular windows in Fig. 5 are large), the numerical rank of the corresponding linear systems will be smaller. An excessive zero assumption forces incorrect zeros into certain regions of the solution. For example, since *in vivo* data are always noisy, applying a zero assumption even in the stationary region of the FOV will cause noise amplification in support regions [22]. In reality, it is difficult to achieve sufficient conditioning and a completely accurate zero assumption. From our experience, using an insufficient zero assumption with insufficient conditioning produces more robust results than using an excessive assumption with sufficient conditioning. During implementation, we manually specified the shape of the zero assumption by referring to the signal distribution in xyf space obtained from the sliding window reconstruction. Support regions were made larger than the distribution from the sliding window reconstruction which underestimates high temporal frequency components. Automatically determining proper shapes of support regions is still an open question and will be application dependent.

The computational complexity of the CG method employed in the proposed method is of practical importance. In the *in vivo* studies, we observe that CG converges at around eight iterations for one set of linear equations, which should be repeated $L/2$ times for whole sets of systems. One design parameter affecting the convergence rate is the extent of the support region in $I^{(l)}$. If it becomes large, the corresponding system will be more ill posed, which will increase the required number of iterations. The regularization coefficient ρ is another parameter that influences the convergence rate. A large ρ increases the values of the diagonal elements of the regularized system matrix [refer to (10)], decreasing the matrix condition number, and vice versa. In the *in vivo* studies we used the coefficient value

$\rho = 0.01$, which is 0.46% of the temporal dc values averaged over the FOV. We observe that when $\rho = 0.001$ is used instead, the required number of iterations becomes around 16 with little change in image quality. When a larger value $\rho = 0.1$ is used, the iteration number is reduced to 4, but the restored images are smoothed more.

One assumption used in the analysis of the aliasing from spiral undersampling is that a group of interleaves are collected at the same time, which is not true. The analytic model used in this paper will be less accurate when larger numbers of interleaves are combined to produce a single time frame. In fact, the true distribution of aliased signals in xyf space can be obtained by considering a single spiral acquisition as a single time frame. Combining a set of spiral interleaves is equivalent to applying sinc weighting followed by aliasing along the frequency dimension. The dilation of the sinc function is determined according to the number of interleaves combined into a single time point. Of course, the system equations derived without combining interleaves will be the most accurate, but in this case the highest temporal frequency to be resolved becomes larger without the increase in system rank. The tradeoff between the accuracy of system equations and the increased dimensionality of the solution needs to be explored in future works.

The twofold acceleration covered in this paper might be a trivial example considering the involved numerical complexity of the proposed approach. The same problem can be solved via UNFOLD-like filtering which is free from an algebraic inversion, as shown in Section IV. The numerical simulation showed that filtering produces subtle increases in rms error, and more apparent increases in maximum error, which can be explained by the regularization effects of the proposed method. The *in vivo* study showed that the reduction of motion blur and background

whirling with the proposed method is comparable to filtering. Still, twofold acceleration is not the ultimate goal and should be considered as a simple example to test the proposed algebraic model. One advantage of the proposed approach is its capability of being fused with any acceleration method based on algebraic operation, for example non-Cartesian sensitivity encoding [23]. Any arbitrary sampling scheme (arbitrary k-space trajectory and arbitrary view ordering) can be handled within the proposed algebraic framework.

VI. CONCLUSION

We have developed a reconstruction method for accelerating dynamic spiral MRI, which is based on the algebraic formulation of aliasing in xyf space. Aliasing from m-fold undersampling is formed such that only m temporal frequencies are coupled to the same set of ill posed linear equations. Each ill posed system can be solved independently assuming a finite support region in the solution. Numerical simulation and *in vivo* experiments using spiral twofold undersampling demonstrate that the proposed method reduces motion blur and motion artifacts due to increased temporal resolution.

The reduction of motion artifacts and motion blur achieved using the proposed method is comparable to but slightly larger than UNFOLD-like filtering, which is computationally more efficient. However, the proposed algebraic framework has the potential to incorporate additional acceleration techniques based on linear operations, such as non-Cartesian sensitivity encoding. The proposed method also benefits from the flexibility to handle arbitrary k-space trajectories, arbitrary acquisition orders, and arbitrary data dimensionality.

ACKNOWLEDGMENT

REFERENCES

[1] R. I. Pettigrew, J. N. Oshinski, G. Chatzimavroudis, and W. T. Dixon, "MRI techniques for cardiovascular imaging," *J. Magn. Reson. Imag.*, vol. 10, pp. 590–601, 1999.

[2] J. P. Earls, V. B. Ho, T. K. Foo, E. Castillo, and S. D. Flamm, "Cardiac MRI: Recent progress and continued challenges," *J. Magn. Reson. Imag.*, vol. 16, pp. 111–127, 2002.

[3] K. S. Nayak and B. S. Hu, "The future of real-time cardiac magnetic resonance imaging," *Curr. Card. Rep.*, vol. 7, pp. 45–51, 2005.

[4] D. C. Noll, D. G. Nishimura, and A. Macovski, "Homodyne detection in magnetic resonance imaging," *IEEE Trans. Med. Imag.*, vol. 10, no. 2, pp. 154–163, Jun. 1991.

[5] K. P. Pruessmann, M. Weiger, M. B. Scheidegger, and P. Boesiger, "SENSE: Sensitivity encoding for fast MRI," *Magn. Reson. Med.*, vol. 42, pp. 952–962, 1999.

[6] D. K. Sodickson and W. J. Manning, "Simultaneous acquisition of spatial harmonics (SMASH): Fast imaging with radiofrequency coil arrays," *Magn. Reson. Med.*, vol. 38, pp. 591–603, 1997.

[7] M. A. Griswold, P. M. Jakob, R. M. Heidemann, M. Nittka, V. Jellus, J. Wang, B. Kiefer, and A. Haase, "Generalized autocalibrating partially parallel acquisitions (GRAPPA)," *Magn. Reson. Med.*, vol. 47, pp. 1202–1210, 2002.

[8] J. J. van Vaals, M. E. Brummer, W. T. Dixon, H. H. Tuithof, H. Engels, R. C. Nelson, B. M. Gerety, J. L. Chezmar, and J. A. den Boer, "Keyhole method for accelerating imaging of contrast agent uptake," *J. Magn. Reson. Imag.*, vol. 3, pp. 671–675, 1993.

[9] R. A. Jones, O. Haraldseth, T. B. Muller, P. A. Rinck, and A. N. Oksendal, "K-space substitution: A novel dynamic imaging technique," *Magn. Reson. Med.*, vol. 29, pp. 830–834, 1993.

[10] A. G. Webb, Z.-P. Liang, R. L. Magin, and P. C. Lauterbur, "Applications of reduced-encoding MR imaging with generalized-series reconstruction (RIGR)," *J. Magn. Reson. Imag.*, vol. 3, pp. 925–928, 1993.

[11] X. Hu and T. Parrish, "Reduction of field of view for dynamic imaging," *Magn. Reson. Med.*, vol. 31, pp. 691–694, 1994.

[12] H. Sedarat, A. B. Kerr, J. M. Pauly, and D. G. Nishimura, "Partial-FOV reconstruction in dynamic spiral imaging," *Magn. Reson. Med.*, vol. 43, pp. 429–439, 2000.

[13] M. E. Brummer, D. Moratal-Perez, C.-Y. Hong, R. I. Pettigrew, J. Millet-Roig, and W. T. Dixon, "Noquist: Reduced field-of-view imaging by direct Fourier inversion," *Magn. Reson. Med.*, vol. 51, pp. 331–342, 2004.

[14] B. Madore, G. H. Glover, and N. J. Pelc, "Unaliasing by Fourier-encoding the overlaps using the temporal dimension (UNFOLD), applied to cardiac imaging and fMRI," *Magn. Reson. Med.*, vol. 42, pp. 813–828, 1999.

[15] J. Tsao, "On the UNFOLD method," *Magn. Reson. Med.*, vol. 47, pp. 202–207, 2002.

[16] J. Tsao, P. Boesiger, and K. P. Pruessmann, "k-t BLAST and k-t SENSE: dynamic MRI with high frame rate exploiting spatiotemporal correlations," *Magn. Reson. Med.*, vol. 50, pp. 1031–1042, 2003.

[17] Q. S. Xiang and R. M. Henkelman, "K-space description for MR imaging of dynamic objects," *Magn. Reson. Med.*, vol. 29, pp. 422–428, 1993.

[18] M. S. Hansen, C. Baltes, J. Tsao, S. Kozerke, K. P. Pruessmann, and H. Eggers, "k–t BLAST reconstruction from non-Cartesian k–t space sampling," *Magn. Reson. Med.*, vol. 55, pp. 85–91, 2006.

[19] C. H. Meyer, B. S. Hu, D. G. Nishimura, and A. Macovski, "Fast spiral coronary artery imaging," *Magn. Reson. Med.*, vol. 28, pp. 202–213, 1992.

[20] S. J. Riederer, T. Tasciyan, F. Farzaneh, J. N. Lee, R. C. Wright, and R. J. Herfkens, "MR fluoroscopy: Technical feasibility," *Magn. Reson. Med.*, vol. 8, no. 1, pp. 1–15, 1988.

[21] K. S. Nayak, B. A. Hargreaves, B. S. Hu, D. G. Nishimura, J. M. Pauly, and C. H. Meyer, "Spiral balanced steady-state free precession cardiac imaging," *Magn. Reson. Med.*, vol. 53, pp. 1468–1473, 2005.

[22] S. K. Plevritis and A. Macovski, "Spectral extrapolation of spatially bounded images," *IEEE Trans. Med. Imag.*, vol. 14, no. 3, pp. 487–497, Sep. 1995.

[23] K. P. Pruessmann, M. Weiger, P. Bornert, and P. Boesiger, "Advances in sensitivity encoding with arbitrary k-space trajectories," *Magn. Reson. Med.*, vol. 46, no. 4, pp. 638–651, 2001.